# High-Density Sodium and Lithium Ion Battery Anodes from Banana Peels

**Elmira Memarzadeh Lotfabad,[†,‡,*] Jia Ding,[†,‡] Kai Cui,[‡] Alireza Kohandehghan,[†,‡] W. Peter Kalisvaart,[†,‡] Michael Hazelton,[†,‡] and David Mitlin[†,‡,*]**

[†]Department of Chemical & Materials Engineering, University of Alberta, 9107 116th Street, T6G 2 V4, Edmonton, Alberta, Canada, and [‡]National Institute for Nanotechnology (NINT), National Research Council of Canada, Edmonton, Alberta, T6G 2M9, Canada

**ABSTRACT** Banana peel pseudographite (BPPG) offers superb dual functionality for sodium ion battery (NIB) and lithium ion battery (LIB) anodes. The materials possess low surface areas (19–217 $m^2\ g^{-1}$) and a relatively high electrode packing density (0.75 g $cm^{-3}$ *vs* ~1 g $cm^{-3}$ for graphite). Tested against Na, BPPG delivers a gravimetric (and volumetric) capacity of 355 mAh $g^{-1}$ (by active material ~700 mAh $cm^{-3}$, by electrode volume ~270 mAh $cm^{-3}$) after 10 cycles at 50 mA $g^{-1}$. A nearly flat ~200 mAh $g^{-1}$ plateau that is below 0.1 V and a minimal charge/discharge voltage hysteresis make BPPG a direct electrochemical analogue to graphite but with Na. A charge capacity of 221 mAh $g^{-1}$ at 500 mA $g^{-1}$ is degraded by 7% after 600 cycles, while a capacity of 336 mAh $g^{-1}$ at 100 $mAg^{-1}$ is degraded by 11% after 300 cycles, in both cases with ~100% cycling Coulombic efficiency. For LIB applications BPPG offers a gravimetric (volumetric) capacity of 1090 mAh $g^{-1}$ (by material ~2200 mAh $cm^{-3}$, by electrode ~900 mAh $cm^{-3}$) at 50 mA $g^{-1}$. The reason that BPPG works so well for both NIBs and LIBs is that it uniquely contains three essential features: (a) dilated intergraphene spacing for Na intercalation at low voltages; (b) highly accessible near-surface nanopores for Li metal filling at low voltages; and (c) substantial defect content in the graphene planes for Li adsorption at higher voltages. The <0.1 V charge storage mechanism is fundamentally different for Na *versus* for Li. A combination of XRD and XPS demonstrates highly reversible Na intercalation rather than metal underpotential deposition. By contrast, the same analysis proves the presence of metallic Li in the pores, with intercalation being much less pronounced.

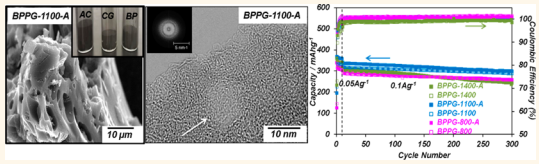


**KEYWORDS:** carbon · graphite · graphene · anode · battery · capacitor · SIB · NIB · NAB

Sodium ion batteries (NIBs, NABs, or SIBs) are highly promising for large-scale energy storage systems (ESS) due to sodium's natural abundance, a more democratic global distribution, and much lower price as compared to Li.[1−4] Graphite microparticles are the standard anode material in commercial lithium ion batteries (LIBs) due to their reasonable reversible capacity (up to 372 mAh $g^{-1}$), low and flat potential plateaus providing an optimum voltage window *versus* an opposing cathode, superior cycling behavior, high Coulombic efficiency, and low cost.[5−8] Unfortunately, conventional graphite is not suitable for NIB anodes.[9−11] Minimal Na ions may be intercalated into graphite, an effect mainly attributed to the larger ionic radii of the Na *versus* Li (0.102 nm *versus* 0.076 nm).[10] Substantial gains have been made to find suitable alternative anode materials for NIBs, including various carbonaceous materials,[12−16] phosphorus,[17,18] ternary ionic sodium compounds,[19−24] metal oxides,[25−30] metal nitrides,[31] alloys,[32−44] graphene, and graphene-based composites.[45,46] An emerging strategy for Li ion batteries is to employ dense, low surface area materials that can store charge by rapid intercalation of ions between the atomic layers, analogous to graphite but with much higher charge storage capacity. This approach has been recently utilized to create a large family of high-performance 2D LIB anode materials, labeled "MXenes" where M is a transition metal and X is C or N.[47−50] Such an approach would be similarly beneficial for NIB applications but has to date not received the same level of scientific attention.

Carbons, along with various earth abundant oxides, are highly attractive for both NIBs and LIBs since in many forms they optimize both performance and cost.[12,51−54] High surface area nanostructured carbons have been utilized for Na storage.[51,52,55] Studies have focused on hard (poorly or non-graphitizable) carbons due to their large interlayer distance, which can accommodate Na insertion in a range of chemically and physically dissimilar storage sites.[51,52,55−57] Emerging approaches include porous cellulose

* Address correspondence to memarzad@ualberta.ca, 780-566-8695, dmitlin@ualberta.ca.

Received for review April 12, 2014 and accepted June 4, 2014.

**Published online June 04, 2014**
**10.1021/nn502045y**

fibers,[58,59] graphene foam,[60] hierarchical structures based on a combination of graphene, carbon nanotubes, and iron nanoparticles,[61] $Fe_2O_3$/graphene hybrids,[62] or highly reversible spherical carbons.[63] Additional noteworthy examples of high-performance NIB carbons include refs 12, 51, 52, 54, 56, 64, and 65. Such materials are very promising from a specific capacity and rate capability viewpoint. However, in many cases the heterogeneous environment of the stored Na creates a distribution of site energies, with "supercapacitor-like" sloping voltage profiles that may be nonideal for some applications. The highest free energy sites in the carbon will trap Na irreversibly or will require a substantial overpotential to have it extracted. This leads to poor cycling Coulombic efficiency and large (1 V or higher) charge/discharge voltage hysteresis.

Bananas are the most commonly eaten fruit in the United States, making up more than 50% of total amount of fruit consumed per year. According to 2009 statistics, approximately 3.5 of the total 6 million metric tons were bananas.[66] The banana peels, which make up 40% of the total weight of the fruit, are inedible to humans and serve little economic purpose apart from being ground into compost along with other biodegradable wastes. The majority of banana peels are placed in landfills or garbage dumps, where they release $CO_2$ along with noxious gases as they decay. In that sense they are an ideal precursor for value-added carbons, possessing a negative value associated with their disposal. Banana peels have been employed to fabricate conventional activated carbons (AC) for wastewater treatment[67−69] and for supercapacitor applications where they also served as a template for aminophenol furfural resin-zinc complexes.[70,71]

In this study we set out to create a NIB carbon that behaves electrochemically like graphite in LIBs. This requires a fundamentally different structure as compared to that of a commercial high surface area, highly disordered AC. While such a material will never hold as much charge (by weight) as ultra-high surface area carbons such as defective or N-doped graphene,[72−74] it will demonstrate key commercial advantages such as (a) maximizing the voltage window of a fuel cell due to a low and flat plateau; (b) being volumetrically dense with a low surface area, resulting in excellent electrode packing characteristics, a high volumetric capacity, and low levels of SEI formation, and (c) being highly reversible with nearly 100% cycling Coulombic efficiency and minimal voltage hysteresis. Our facile synthesis strategy combined with a precursor that is truly an abundant waste will make these electrodes both inexpensive and environmentally friendly.

## RESULTS AND DISCUSSION

**Structure of BPPG and BPPG-A.** We employ a shorthand designation to label the various carbons. The as-pyrolyzed banana peel pseudographite is named BPPG-*x*, with *x* representing the carbonization temperature. The subsequently air-activated carbon is termed BPPG-*x*-A. Battery-grade graphite, labeled CG, and high surface area, high electrical conductivity activated carbon, labeled AC (both commercially purchased), were employed as baselines.

The heterogeneous structure of a banana peel consists of biopolymers in plant cell walls and includes hemicelluloses, pectins, lignins, free sugars, proteins, and some crystalline cellulose.[75] Both hemicellulose and lignin are highly cross-linked and noncrystalline, thus favoring formation of nongraphitic carbons at reasonable pyrolysis temperatures. Lignin is deemed especially important for converting biomass into porous carbons through pyrolysis.[76] The banana peels contain up to 20% pectin, which is another branched biopolymer molecule, being similar in structure to lignin and consisting of sugar monomers. Up to 35% of the peel dry mass is made up of free sugars, although the exact composition varies between species and with ripening.[75,77] During pyrolysis, organic molecules emit gases such as CO and $CH_4$, while the remaining carbon cross-links and undergoes some aromatic ordering. If the precursor is rich in smaller molecules such as the free sugars, a viscous liquid may form, allowing the graphene sheets to partially align themselves in the pitch that precedes full carbonization.[78] As discussed in the introduction, formation of equilibrium graphite has to be avoided, as the interlayer spacing is too small to facilitate Na intercalation. The banana peel is an ideal precursor for NIB anodes, balancing the lignin and pectin fractions that prevent crystallization of equilibrium graphite with the free sugars that enable partial ordering of the graphene layers. Such pseudographitic ordering allows for significant Na intercalation into the graphene interlayer spacings of the pyrolyzed carbon. However, the resultant graphene sheets are also highly defective (*e.g.*, divacancy and Stone−Wales defects). These reversibly bind to Li and thus allow for 3 times more charge to be stored as compared to equilibrium graphite in LIBs.

Figure S1a (Supporting Information) shows an environmental SEM image of a cross-sectioned dried banana peel. In the as-dried state (precarbonization) the peels are effectively dense with little visible macroporosity. Figures 1a, S1b, and S1c show SEM micrographs of the BPPG specimens. As a result of the pyrolysis, the materials develop limited macroporosity. The inset in Figure 1a compares the density of loose (not tapped) powders of BPPG-1100-A with that of commercial electrode grade graphite (CG) and with commercial supercapacitor electrode-grade activated carbon (AC). With the same sample mass (1.19 g), the packed volume of BPPG-1100-A is substantially lower than that of activated carbon, being closer to that of graphite. Since the diameter (1.9 cm) of the glass vials is identical in each case, the relative densities of the

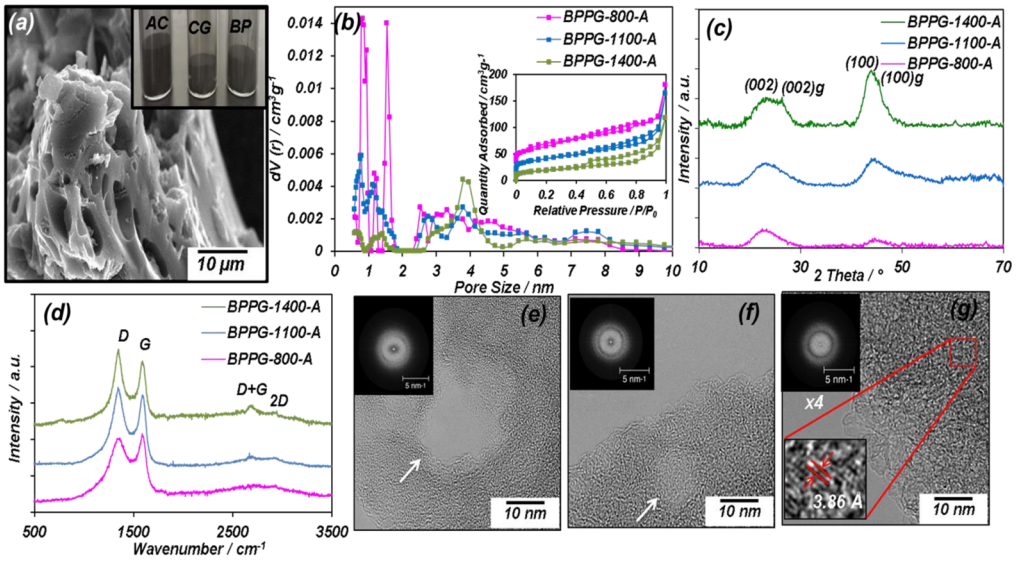


**Figure 1. Structure of banana peel pseudographite (BPPG) in its activated state. (a) SEM micrograph highlighting the general morphology of a BPPG particle (BPPG-1100-A), with the inset showing its volume difference in comparison with baseline commercial graphite (CG) and activated carbon (AC) of the same weight. (b) Pore size distribution (calculated from the adsorption isotherms using the DFT method) with the inset showing nitrogen adsorption−desorption isotherms. (c and d) XRD and Raman spectra. (e−g) HRTEM micrographs of BPPG-800-A, BPPG-1100-A, and BPPG-1400-A, respectively. The corresponding data for BPPG are shown in Figure S2a,b.**

loose powders are effectively the inverse of their packed height difference. The heights of the AC, GC, and BPPG-1100-A powders are 1.2, 0.7, and 0.8 cm, respectively.

Table 1 lists the relevant physical properties of BPPG, BPPG-A, and CAC. The pore size distributions, calculated using the density functional theory (DFT) model from the adsorption branch, are shown in Figure 1b. The actual experimental isotherms for BPPG-A are shown in the inset, which show type-I/IV behavior. Interestingly, increasing the carbonization temperature promotes a shift from microporosity to mesoporosity for an identical air activation treatment (300 °C). For instance after carbonization at 1400 °C, the material is primarily mesoporous, with the largest volume fraction of pores being centered at 3.7 nm. Air activation is known to preferentially attack the disordered (less thermodynamically stable) portions of the carbon. One can argue that with increasing carbonization temperature and the enlargement of the pseudographitic domains (Table 1) there is a concomitant coarsening of the remaining disordered regions. This would lead to larger pores in the postactivated state. For the nonactivated specimens the total surface areas range from 14.5 to 33 $m^2/g$, which is effectively the geometric surface area with an additional contribution from the macroporosity. Even after activation, the surface areas are relatively low, ranging from 62 to 217 $m^2/g$. The true density of the carbons may be estimated as 2 g/(1 $cm^3$ + volume of pores). The total pore volumes for BPPG, BPPG-A, and commercial high surface area activated carbon (AC) are listed in Table 1. While for the BPPG and BPPG-A the resultant density is still in the 2 $g/cm^3$ range, for the case of AC the density is half that value, i.e., 1 $g/cm^3$.

Figure 1c shows the X-ray diffraction (XRD) patterns of BPPG-A. The XRD patterns of the BPPG are shown in Figure S2c. It can be seen that the 300 °C activation will not appreciably alter the graphitic order/disorder. The results of the XRD analysis, along with the results of Raman and BET, are shown in Table 1. The average graphene interlayer spacing was calculated from the peak centers. The thickness and average width of the graphitic domains, $L_c$ and $L_a$, are calculated based on the well-known Scherrer equation, using the fwhm values of (002) at $2\theta \approx 23°$ and (100) at $2\theta \approx 43°$.

As Table 1 demonstrates, the integraphene layer ($d_{002}$) spacing gradually shifts toward lower values with increasing carbonization temperature. However, a comparison of the 800, 1100, and 1400 °C carbons indicates that this trend is quite weak and that in all cases the spacing is significantly above that of equilibrium graphite (0.3354 nm). In the 800 and 1100 °C specimens the average thickness of the pseudographitic domains is ~1.6 nm, indicating that they are composed of ~4 stacked graphene layers (*i.e.*, 1.6/0.4 = 4). In the 1400 °C specimens the domains are composed of ~5 stacked layers. Carbonizing at 1400 °C creates a bimodal distribution in the average *d* spacings, indicating that the temperature is finally high enough to form equilibrium graphite (*c*/2 measured as 0.3354 nm). The two overlapping peaks were mathematically deconvoluted using the Voigt function. On the basis of the deconvoluted areas of the peak doublets, the carbon to equilibrium graphite ratio for BPPG-1400-A is 8:1 by weight.

**TABLE 1. Structure and Textural Properties of BPPG and BPPG-A**

| sample | $d_{002}$ (Å) | $L_a$ (nm) | $L_c$ (nm) | $I_G/I_D$[a] | $S_{BET}$ ($m^2/g$)[b] | $V_t$ ($cm^3/g$)[c] | pore vol % (<2 nm) | pore vol % (>2 nm) |
|---|---|---|---|---|---|---|---|---|
| BPPG-800 | 3.97 | 2.12 | 1.56 | 0.78 | 33.0 | 0.059 | 20.3 | 79.7 |
| BPPG-1100 | 3.91 | 4.15 | 1.59 | 0.91 | 19.3 | 0.052 | 10.1 | 89.9 |
| BPPG-1400 | 3.84/3.35 | 7.30/10.91 | 2.04/5.56 | 0.93 | 14.5 | 0.047 | 6.2 | 93.8 |
| BPPG-800-A | 3.99 | 2.43 | 1.59 | 0.79 | 217.3 | 0.23 | 55.4 | 44.6 |
| BPPG-1100-A | 3.92 | 4.36 | 1.62 | 0.92 | 130.8 | 0.19 | 38.2 | 61.8 |
| BPPG-1400-A | 3.86/3.35 | 7.43/11.31 | 2.12/5.49 | 0.94 | 62.1 | 0.14 | 13.8 | 86.2 |
| AC | 3.72 | 4.2 | 1.84 | 0.26 | 2050 | 1.17 | 61.7 | 38.3 |

[a] $I_D$ and $I_G$ are the integrated intensities of the D and G band. [b] Surface area was calculated with Brunauer–Emmett–Teller (BET) method. [c] The total pore volume was determined at a relative pressure of 0.98.

Raman spectroscopy analysis results are shown in Figure 1d and Figure S2d. In a Raman spectrum for carbon materials the G band is a characteristic feature of the graphitic layers and corresponds to the tangential vibration of the carbon atoms, while the D band corresponds to disordered carbon or defective graphitic structures. The integral intensity ratio of these two peaks scales with the degree of graphitic ordering in the carbons.[79] The integral intensity ratio of G band to D band rises with increasing carbonization temperature, agreeing with the XRD results. The fits of the spectra are shown in Figure S3 (Supporting Information), with the resultant $I_G/I_D$ being shown in Table 1. For all synthesis conditions, the $I_G/I_D$ ratio never goes above 1, indicating that the ordered graphene sheets in all the materials are highly defective.

High-resolution transmission electron microscopy (HRTEM) micrographs of BPPG-800-A, BPPG-1100-A, and BPPG-1400-A are shown in Figure 1e–g. For all three materials, well-defined larger (~3 nm and upward) mesopores were observed throughout the structure, with individual ones being shown by arrows in Figure 1e and f. The HRTEM micrographs show a speckled contrast synonymous with the presence of microporosity. However, due to the inevitable overlap of the individual sub-2 nm pores with the carbon along the beam path, it is not possible to resolve the micropores within the images. The HRTEM micrographs also show that with increasing carbonization temperature there is more aromatic ordering, agreeing with the XRD and the Raman results.

Figure S4 and Tables S1 and S2 present X-ray photoelectron spectroscopy (XPS) results for BPPG and BPPG-A specimens. XPS data shown in Table S1 were from analysis performed on as-synthesized carbons. Table S2 shows XPS results on carbons that were mechanically ground after synthesis so as to expose bulk material to surface analysis. Combustion elemental analysis was also employed to obtain the bulk N, H, and O content, the results being listed in Table S1. From both sets of XPS results it can be concluded that BPPG and BPPG-A contain nitrogen (0.48–2.82 wt %) and oxygen (5.55–9.31 wt %) heteroatoms, with minor amounts of Si (0.1–1.45 wt %), Cl (0.14–0.38 wt %), K (0.1–0.82 wt %), Mg (0.1–0.17 wt %), and P (0.06–0.13 wt %). Elements K, Mg, and P were detected only after grinding the powders, indicating that they are depleted from the as-synthesized near-surfaces. Activation does somewhat increase the surface oxygen content of the materials, especially for the sample that was pyrolized at 800 °C. Since the carbons had low surface areas (19–217 $m^2/g$), it is not expected that O and N surface functionalities will have an appreciable impact on the electrochemical performance.

**Electrochemical Performance *versus* Na.** We performed cyclic voltammetry (CV) and galvanostatic discharge/charge cycling on both the BPPG and BPPG-A, as well as on CAC, tested between 0.001 and 2.8 V *versus* $Na/Na^+$. Figure 2a and b show the CV curves and the galvanostatic discharge/charge profiles for BPPG-1100-A, at cycle 1, 2, 5, and 10. The CV and galvanostatic data for the other materials are shown in Figures S5 and S6. The inset in Figure 2b is the d*Q*/d*V* curve, which has a similar shape to the CVs. Two small reduction peaks at ~0.5 and ~0.7 V are observed in the first CV scan and disappeared in the subsequent scans. The formation of a solid electrolyte interface (SEI) would occur at these potentials. However, due to the carbons' low surface area, we attribute these two peaks more to irreversible Na insertion into the bulk. Table S3 shows the cycle 1 Coulombic efficiency (CE) of BPPG and BPPG-A. There is a notable improvement in the cycle 1 CE with increasing order in the carbons (going from 63% to 73% for 800 °C *versus* 1400 °C carbonization) but only a marginal decrease in the CE with increased surface area (*e.g.*, dropping to 61% for 800 °C + activation). This indicates the cycle 1 irreversible trapping of Na is associated with carbon disorder, be it at the highly defective graphene sites or in the amorphous regions between the pseudographitic domains. However, during steady-state cycling the CE is 100%; hence minimal additional permanent trapping of Na occurs.

A pair of highly reversible (minimal voltage hysteresis) oxidation/reduction peaks are present at 0.3–0.01 V, similar to lithium insertion into graphite.[5,7] As Table S3 points out, at an intermediate charging rate (50 mA $g^{-1}$) the reversible capacity of the as-carbonized

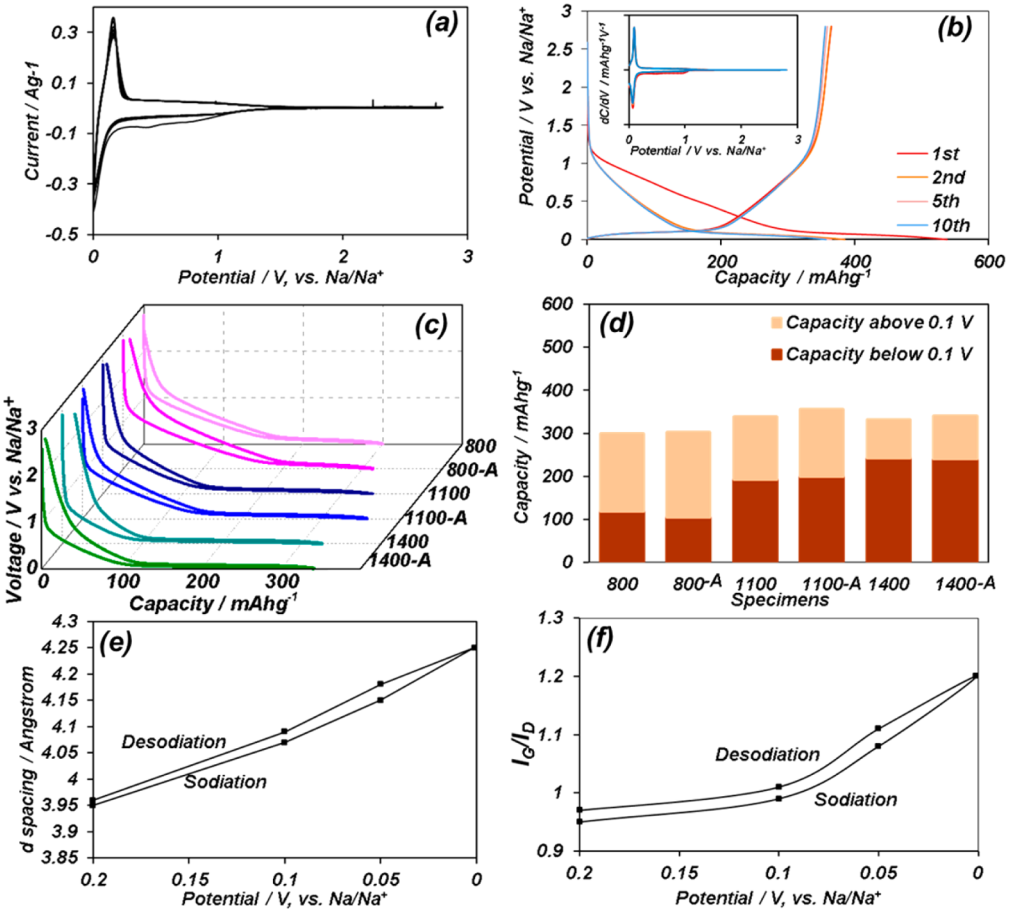


**Figure 2. Electrochemical performance of BPPG tested in a half-cell against Na. (a) Cyclic voltammogram (CV) of BPPG-1100-A tested at 0.1 mV $s^{-1}$. (b) Galvanostatic discharge/charge curves of BPPG-1100-A at a current density of 50 mA $g^{-1}$. (c) Potential profiles of BPPG and BPPG-A electrodes. (d) Summary of capacity above and below 0.1 V in BPPG and BPPG-A, 10th cycle at 50 mA $g^{-1}$. (e) Dependence of the mean graphene interlayer spacing of BPPG-1400-A on discharge/charge voltage, demonstrating reversible Na intercalation-induced dilation of the mean intergraphene spacing. The electrodes were galvanostatically discharged/charged to 0.2, 0.1, 0.05, and 0.001 V, with dilation values derived from XRD spectra shown in Figures S8. (f) Raman integral intensity ratio ($I_G/I_D$) of BPPG-1400-A as a function of discharge/charge voltage, demonstrating intercalation-induced ordering of the carbon; values derived from Raman spectra in Figure S8.**

and the activated specimens is very similar. For instance, for BPPG-1100 *versus* BPPG-1100-A the total capacity difference is 23 mAh $g^{-1}$ (362 *versus* 385 mAh $g^{-1}$). As Figure 2c shows, all the BPPG and BPPG-A display a sloping-voltage region and a nearly flat plateau at potentials lower than 0.2 V. The effect of carbonization temperature on the fraction of the total capacity associated with the plateau below 0.1 V is summarized in the histogram shown in Figure 2d. The sub-0.1 V capacities increase with higher degree of ordering, being 106 mAh $g^{-1}$ for BPPG-800-A, 200 mAh $g^{-1}$ for BPPG-1100-A, and 238 mAh $g^{-1}$ for BPPG-1400-A. The low-voltage capacity is fully independent of activation, indicating that it is not due to nanopore filling by Na metal, *aka* "nanoplating".

Charge storage in carbons for LIBs and NIBs has been ascribed to the following mechanisms: chemisorption on surface heteroatoms,[80] metal nanopore filling, *i.e.*, "nanoplating",[52,78,81] intercalation between graphene layers,[12,54] and reversible adsorption at structural defect sites in the graphene.[82−86] The charge−discharge profiles in high surface area carbons with high O and N contents have a substantial voltage hysteresis, often being on the order of 1 V or more throughout the entire capacity range.[56,57,80] Below 0.2 V the 1100 and 1400 °C BPPG and BPPG-A have hysteresis that is less than 0.05 V. As we will demonstrate in the subsequent analysis, the key low-voltage charge storage mechanism for BPPG is the reversible intercalation of Na between the graphene planes of the pseudographitic domains. In all the BPPG specimens the graphene sheets also contain a high content of defects. We attribute the sloping high-voltage charge storage behavior to reversible binding of Na at graphene divacancies and Stone−Wales defects, as has been recently predicted by *ab initio* calculations.[83]

The relatively high density of BPPG also delivers a high volumetric charge storage capacity. Figure S7 provides this result for BPPG-1100-A, as a function of cycle number. For all experiments we employed a mass loading of ~1 mg/$cm^2$, giving an average electrode thickness of 14 $\mu$m (see cross section SEM image in

Figure S7). This results in an electrode with a packing density of ~0.75 g $cm^{-3}$. Thus, the reversible volumetric capacity obtained for BPPG-1100-A is ~700 mAh $cm^{-3}$ by active material (*i.e.*, based on the true density of the carbon) and ~270 mAh $cm^{-3}$ by electrode volume. It is difficult to make a one-to-one volumetric comparison with commercial LIB graphite since professionally manufactured commercial electrodes are both thicker (with correspondingly higher mass loading) and roll-pressed rather than drop-cast onto a current collector. The details of the manufacturing process are almost always proprietary. However, it is possible to increase the packing density and the mass loading of BPPG to be closer to commercial systems. We employed a Carver laboratory press (4000 psi) to achieve electrodes with a mass loading of ~6.2 mg. The resultant electrode thickness was 39 $\mu$m on a geometric area of 1.54 $cm^2$. This electrode is also shown in Figure S7.

We employed XRD and Raman spectroscopy to further understand the changes that occur in BPPG-1400-A during Na insertion/extraction. The results are shown in Figure 2e and f, with the raw data being presented in Figure S8a and b. To obtain a "steady-state" microstructure, the half-cells first received 10 galvanostic charge/discharge cycles at 30 mA $g^{-1}$. Upon cycle 11, the electrodes were discharged to (a) 0.2, (b) 0.1, (c) 0.05, and (d) 0.001 V and then charged to (e) 0.05 V, (f) 0.1 V, and (g) 0.2 V. The cells were then disassembled in a glovebox with the active material being removed from the current collector, cleaned, and immediately analyzed. Figure 2e shows a plot of the mean *d* spacing *versus* voltage. The broad (002) pseudographitic peak shifts to lower angles as the electrode is sodiated. The *d* spacing is progressively expanded from the initial 3.96 Å to the final 4.25 Å at 0.001 V. The measured dilation has to be due to Na intercalation between the graphene layers, similar to Li in graphite. It has been reported that the equilibrium interplanar distance for $NaC_6$ is about 0.45 nm, while that for $LiC_6$ is 0.37 nm.[52,87] On the basis of the capacity achieved at this cycle number (~330 mAh $g^{-1}$), the stoichiometric factor *x* in $Na_xC_6$ is ~0.88. Examining the interlayer upon subsequent desodiation indicates that the process is highly reversible, agreeing with the electrochemical testing. As indicated by the Raman spectra (Figure 2f), BPPG-1400-A becomes progressively more ordered during sodiation and subsequently disordered during the reverse process. Similar to the XRD results, the ordering is highly reversible with voltage. This Na insertion-induced ordering phenomenon has not been previously reported.

Neither XRD nor XPS shows evidence of Na metal nanopore filling even at 0.001 V. Metal peaks were not detected in the XRD patterns for any of the BPPG. We followed the XPS–Scotch tape methodology employed in ref 84 to analyze Na bonding in the interior of BPPG-1400-A. The C 1s spectrum shown in Figure S8d shows minimal (Na)carbonates, indicating that the SEI layer was successfully removed along with the top of the carbon. Figure S8c demonstrates a strong binding peak of Na at 1071.1 eV, which almost entirely disappears at 2.8 V. We attribute this peak to C–Na bonds within the pseudographitic domains, although prior experimental evidence for this interpretation is unavailable. The binding energy for metallic sodium is 1071.7 eV, while for $Na_2O$ it is 1072.5 eV,[88] both of which are conspicuously absent. The fact that the Na signal almost entirely disappears at 2.8 V is also a strong indication that the SEI is removed. XPS results on samples without using the Scotch tape approach show a strong peak in Na 1s spectra at ~1071 eV at both 0.001 and 2.8 V but with lower signal intensity after desodiation to 2.8 V. This indicates that some of the decomposition products that are formed can be partially dissolved. The presence of considerable (Na)carbonate peaks after desodiation to 2.8 V in both Na 1s and C 1s spectra indicates that these peaks could be related to the decomposition products rather than Na inside the electrode. This was further confirmed by SEM images of electrodes after desodiation to 2.8 V before and after using the Scotch tape method (Figure S9). The morphology of the electrode after using the Scotch tape method is almost identical to the as-prepared one with clean surfaces and sharp boundaries. By contrast, without using this method the surface is no longer smooth but rather rough in appearance, with an SEI layer covering the surface.

Figure 3a shows the cycling capacity retention performance of BPPG-A and BPPG, tested at 50 mA $g^{-1}$ for the first 10 cycles and at 100 mA $g^{-1}$ for the next 290 cycles. The BPPG-1100-A and BPPG-1100 electrodes show the best combination of total capacity and capacity retention. BPPG-1100-A and BPPG-1100 possess a reversible capacity of 339 and 318 mAh $g^{-1}$ at cycle 11 and 298 and 286 mAh $g^{-1}$ at cycle 300. In BPPG-800, BPPG-800-A, BPPG-1100, and BPPG-1100-A the Coulombic efficiency increases dramatically upon cycling, reaching over 98% after 5 cycles and ~100% (within measurement accuracy of the instruments) after 10 cycles. BPPG-1400-A and BPPG-1400 demonstrate slightly lower cycling CE (98.5–99%) and degrade faster during cycling than the rest. The cycle 11 capacities of BPPG-1400-A and BPPG-1400 are 310 and 295, respectively. After 300 cycles these numbers are reduced to 240 and 242, *i.e.*, 22% and 18% degradation. We believe that both the lower CE and the faster degradation are related to the presence of the secondary graphite phase. Upon attempted insertion of the misfitting Na ions, the graphite begins to exfoliate, creating new surfaces and resulting in limited local pulverization of the electrode. Any fresh surfaces exposed to electrolyte will cause new SEI formation and subsequent loss of cycling CE, while local pulverization

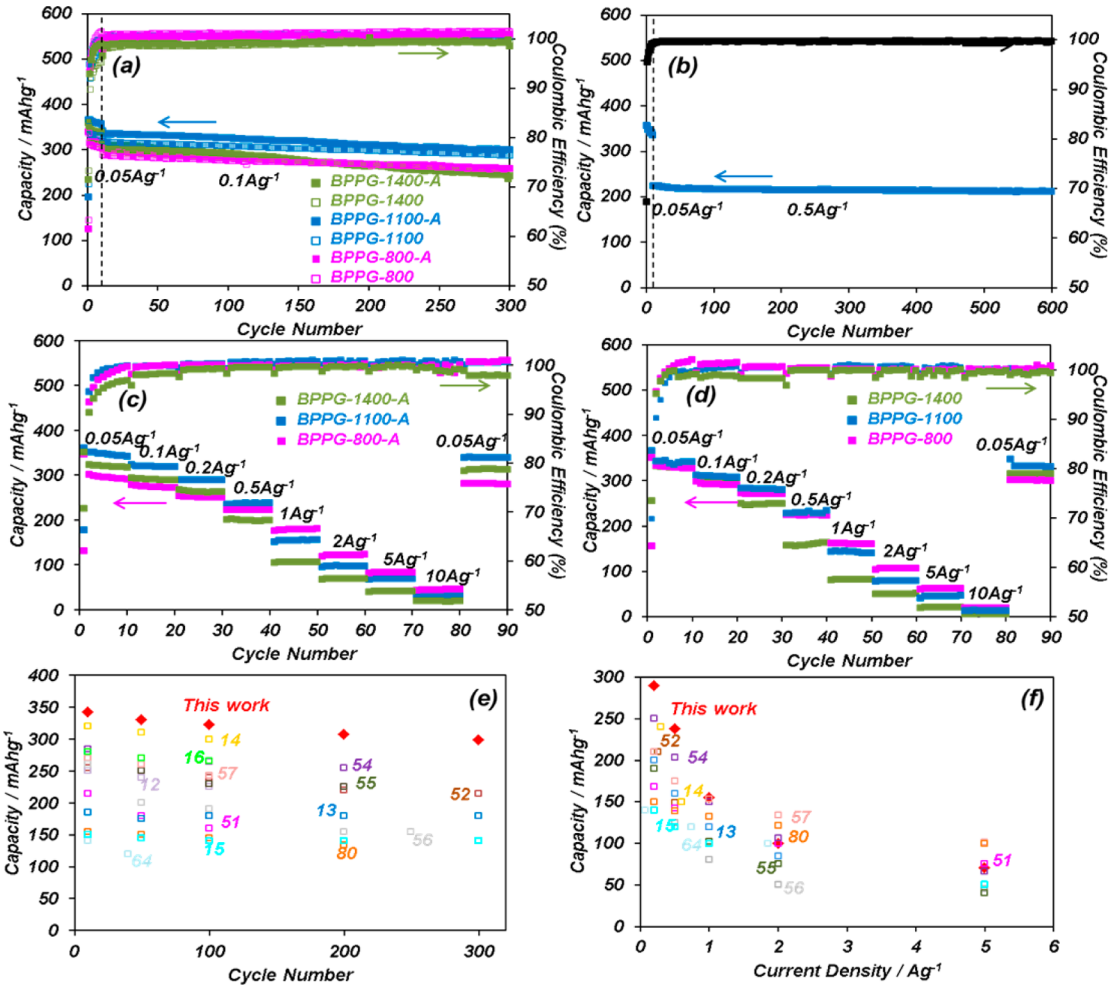


**Figure 3. (a) Cycling performance of the BPPG and BPPG-A electrodes tested in a half-cell against Na, with the corresponding Coulombic efficiency (CE) being displayed on the right axis. (b) Extended cycling performance and CE of the BPPG-1100-A electrode. (c) Rate performance of BPPG-A electrodes. (d) Rate performance of BPPG electrodes. (e, f) Cycling capacity retention and rate capability comparison of BPPG-1100-A with the state-of-the-art in the literature, tested *versus* Na. Red diamonds are our results.**

would lead to a capacity decay due to loss of electrical contact. We cycled the best overall performing material (BPPG-1100-A) up to 600 cycles at a rate of 500 mA $g^{-1}$. These results are also shown in Figure 3b. The electrode exhibits a stable capacity of 210 mAh $g^{-1}$ at cycle 600, corresponding to a capacity retention of 93%. It also demonstrates a cycling CE of ~100%.

A comparison of Figure 3c and d highlights the effect of activation on the electrodes' high rate capability. For a given carbonization treatment, at low and moderate rates the positive effect of activation is quite minor. However, at high rates (*e.g.*, 5 and 10 A $g^{-1}$) the activated specimens outperform the nonactivated ones. BPPG-1400-A and BPPG-1400 possess the overall smallest surface areas and pore volumes and demonstrate the lowest capacities at rates 0.5 A $g^{-1}$ and above. BPPG-800 and BPPG-800-A possess by far the largest surface areas and pore volumes and offer the highest capacity at 1 A $g^{-1}$ and above. For the reasons previously discussed, BPPG-1100-A and BPPG-1100 show the best performance at moderate (0.5 A $g^{-1}$ is about 1.5C) and low rates. However, these specimens possess surface areas and pore volumes lower than BPPG-800/BPPG-800-A, placing them at a high rate disadvantage. These rate trends may be explained by considering the role of activation in introducing porosity in each of the materials and the subsequent role of porosity in reducing solid-state Na diffusion distances within the carbons. It is reasonable to assume that at higher charging/discharging rates the extent of sodiation will become solid-state diffusion limited. This is a key difference between batteries and electrical double layer (EDL) capacitors, where in the latter case the ion diffusional limitations will occur within the electrolyte.[58,89] Assuming electrolyte contact on both sides of a carbon wall, the Na diffusion distance may be approximated as half the wall thickness. The introduction of limited micro- and mesoporosity into the BPPG is therefore essential for reducing the solid diffusional limitations by creating carbon walls that are in effect much thinner than their macroscopic dimensions.

Electrochemical impedance spectroscopy (EIS) was employed to further examine the cycling behavior of BPPG-A and BPPG. The impedance spectra of the electrodes before and after cycling were modeled with the equivalent circuit depicted in Figure S10. Figures S11−S14 show the Nyquist plots for samples before cycling and after 300 cycles, respectively. The spectra consist of a depressed semicircle in the high- and middle-frequency regions and a straight line in the low-frequency region. $R_{el}$ represents the sum of electrical resistances (contacts, *etc.*), $C_{dl}$ the electrical double layer capacitance, $R_{ct}$ the charge transfer resistance, and $Z_W$ the Warburg-type element associated with ion diffusion in the carbon electrode. For the cycled electrodes an additional parallel combination of a resistor and capacitor is added to represent ion transport through the SEI layer,[90] denoted as $R_f$ and $C_f$, respectively. The numerical values obtained from modeling are listed in Table S4.

For the as-prepared samples, the trend in the charge transfer resistance, which is roughly equal to the diameter of the semicircle in the spectra, indicates that the lower carbonization temperature gives higher charge transfer resistance (Figures S11, S12). It is plausible that Na insertion into a more disordered carbon from the electrolyte will be less facile than for a more ordered counterpart. Thus, there would be a higher charge transfer resistance in the as-synthesized state, prior to SEI formation. The cycling-induced increase in the charge transfer resistance is on par for the BPPG-1100-A and BPPG-800-A specimens. However, the total charge transfer resistance of BPPG-800-A remains higher than for BPPG-1100-A, an effect probably associated with the underlying structure of the carbon. As Figure S15e indicates, past the first several charge/discharges, the cycling-induced increase in the charge transfer resistance in both BPPG-1100-A and BPPG-800-A is quite minimal. The EIS results support our interpretation that the electrode's rate capability is dominated by solid-state diffusion of Na inside the carbon, as BPPG-800-A has better rate performance despite having a higher charge transfer resistance than BPPG-1100-A. After 300 cycles the charge transfer resistance is significantly larger for BPPG-1400-A and BPPG-1400 specimens (Figure S13 and Table S4), supporting the argument that the samples' inferior cycling Coulombic efficiency is associated with higher rates of SEI formation.

A comparison of the performance of the BPPG-1100-A specimen with state-of-the-art carbons is presented in Table 2 and in Figure 3e and f. Figure 3e and f show the cycling performance and the rate capability comparison, respectively, with the solid red diamonds being our results. Table 2 emphasizes the plateau capacity (below 0.1 V) comparison of BPPG-1100-A with literature, an essential metric not captured in the total capacity plots presented in Figure 3e and f. Carbons included in the comparison are carbon nanosheets,[52] carbon nanofibers,[13,16,53,57,80] hard carbon,[12,14] templated carbon,[64] highly disordered carbon,[55] hollow carbon nanowires,[52] hollow carbon nanospheres,[51] carbonized peat moss,[54] and nanocellular carbon foams,[15] all of them being primarily high surface area materials. To the best of our knowledge, the combination of high reversible volumetric and gravimetric capacities, the flat low-voltage and low-hysteresis plateaus, the extended cycling performance, and high rate capability have seldom been achieved in previous reports on sodium ion battery anode carbons.

**Electrochemical Performance *versus* Li.** The dense BPPG carbons are also uniquely promising for LIB applications, as the highly defective graphene sheets within the pseudographic domains will reversibly bind with Li, while the near-surface nanopores will provide sites for underpotential metal deposition. Figure 4a shows the cycling performance of the BPPG-A electrodes, with the Coulombic efficiency of the electrodes also being displayed. The cycling CE is close to 100%. Figure 4b shows the rate performance of the BPPG-1100-A electrode. BPPG-800-A, which is the most disordered carbon, demonstrated by far the highest overall cycling capacity, being at 800 mAh $g^{-1}$ at cycle 300 when tested at 100 mA $g^{-1}$. This is direct evidence for the necessity of graphene defects in achieving a reversible capacity with Li that far surpasses that of commercial graphite. It has been shown that a divacancy is the thermodynamically most stable defect[84,91,92] and will also act as a preferential Li adsorption site.[84]

The CV curve of the BPPG-1100-A specimens is shown in Figure S16a. Lithiation/delithiation demonstrates a pronounced reduction peak at 0−1 V during the first cycle and at 0−0.5 V during the subsequent cycles. The discharge−charge profiles for BPPG-A and BPPG are shown in Figures S16 and S17. The initial CEs are slightly lower when employing Li (Table S5) rather than Na (Table S3), which may account for the difference in the structure and in the formation kinetics of SEI.[64,93] The degree of irreversible trapping of Li within the bulk of the carbon would also affect the cycle 1 CE values. Figure S18a compares the capacity *versus* voltage profiles for BPPG and BPPG-A *versus* Li, while Figure S18b shows a summary of capacity *versus* voltage. The galvanostatic profiles are less flat than they are with Na and do show a marked hysteresis. These features are in accord with other reports on Li insertion/extraction into nongraphitic carbons.[52,72,94]

The EIS data for BPPG-1100-A, presented in Figure S15d, show a trend similar to the case of Na. Early during cycling the charge transfer resistance increases somewhat and remains essentially invariant during subsequent testing up to 300 cycles.

There is a major difference in the reversible capacity with Li *versus* with Na, the former being up to 3 times higher. Activation has a substantial effect when testing

**TABLE 2. Plateau Capacity (below 0.1 V) Comparison of BPPG-1100-A *versus* State-of-the-Art NIB Carbons**

| material | initial Coulombic efficiency (%) | plateau capacity (capacity below 0.1 V *vs* $Na/Na^+$) | cyclability (discharge capacity) | rate performance |
|---|---|---|---|---|
| BPPG-1100-A (this work) | 67.8 | 200 mA $g^{-1}$ at 50 mA $g^{-1}$ (10th cycle) | 342 mAh $g^{-1}$ at 11th cycle<br>298 mAh $g^{-1}$ at 300th cycle<br>88% capacity retention over 290 cycles at 100 mA $g^{-1}$ | 290 mAh $g^{-1}$ at 200 mA $g^{-1}$<br>238 mAh $g^{-1}$ at 500 mA $g^{-1}$<br>155 mAh $g^{-1}$ at 1 A $g^{-1}$<br>100 mAh $g^{-1}$ at 2 A $g^{-1}$<br>70 mAh $g^{-1}$ at 5 A $g^{-1}$ |
| carbon nanosheets (ref 56) | 34.8 | *ca.* 40 mAh $g^{-1}$ at 50 mA $g^{-1}$ (10th cycle) | *ca.* 260 mAh $g^{-1}$ at 10th cycle<br>*ca.* 155 mAh $g^{-1}$ at 200th cycle<br>60% retention over 190 cycles at 50 mA $g^{-1}$ | *ca.* 190 mAh $g^{-1}$ at 200 mA $g^{-1}$<br>*ca.* 125 mAh $g^{-1}$ at 500 mA $g^{-1}$<br>*ca.* 80 mAh $g^{-1}$ at 1A $g^{-1}$<br>50 mAh $g^{-1}$ at 2 A $g^{-1}$<br>45 mAh $g^{-1}$ at 5 A $g^{-1}$ |
| interconnected carbon nanofibers (ref 80) | 41.8 | not reported | 151 mAh $g^{-1}$ at 10th cycle<br>134.2 mAh $g^{-1}$ at 200th cycle<br>88.7% retention over 190 cycles at 200 mA $g^{-1}$ | 150 mAh $g^{-1}$ at 200 mA $g^{-1}$<br>139 mAh $g^{-1}$ at 500 mA $g^{-1}$<br>132 mAh $g^{-1}$ at 1 A $g^{-1}$<br>121 mAh $g^{-1}$ at 2 A $g^{-1}$<br>100 mAh $g^{-1}$ at 5 A $g^{-1}$ |
| hard carbon particles (ref 12) | 78 | *ca.* 150 mAh $g^{-1}$ at 25 mA $g^{-1}$ | 250 mAh $g^{-1}$ at 2nd cycle<br>225 mAh $g^{-1}$ at 100th cycle<br>88% retention over 98 cycles at 25 mA $g^{-1}$ | not reported |
| templated carbon (ref 64) | 20 | *ca.* 20 mAh $g^{-1}$ at 74 mA $g^{-1}$ (10th cycle) | 180 mAh $g^{-1}$ at 2nd cycle,<br>120 mAh $g^{-1}$ at 40th cycle<br>66.7% retention over 38 cycles at 74 mA $g^{-1}$ | *ca.*140 mAh $g^{-1}$ at 74 mA $g^{-1}$<br>*ca.*120 mAh $g^{-1}$ at 740 mA $g^{-1}$<br>*ca.* 100 mAh $g^{-1}$ at 1.85 A $g^{-1}$ |
| carbon fibers (ref 57) | 46 | not reported | *ca.* 350 mAh $g^{-1}$ at 2nd cycle<br>243 mAh $g^{-1}$ at 100th cycle<br>70% retention over 98 cycles at 50 mAh $g^{-1}$ | 210 mAh $g^{-1}$ at 200 mA $g^{-1}$<br>175 mAh $g^{-1}$ at 500 mA $g^{-1}$<br>153 mAh $g^{-1}$ at 1 A $g^{-1}$<br>134 mAh $g^{-1}$ at 2 A $g^{-1}$<br>101 mAh $g^{-1}$ at 5 A $g^{-1}$ |
| highly disordered carbon (ref 55) | 57.6 | *ca.* 110 mAh $g^{-1}$ at 100 mA $g^{-1}$ (3rd cycle) | 255 mAh $g^{-1}$ at initial cycles<br>234 mAh $g^{-1}$ at 180th cycle<br>92% retention over 170 cycles at 100 mA $g^{-1}$ | 190 mAh $g^{-1}$ at 200 mA $g^{-1}$<br>139 mAh $g^{-1}$ at 500 mA $g^{-1}$<br>102 mAh $g^{-1}$ at 1 A $g^{-1}$<br>75 mAh $g^{-1}$ at 2 A $g^{-1}$<br>40 mAh $g^{-1}$ at 5 A $g^{-1}$ |
| hollow carbon nanowires (ref 52) | 50.5 | *ca.* 150 mAh $g^{-1}$ at 50 mA $g^{-1}$ (10th cycle) | *ca.* 255 mAh $g^{-1}$ at 10th cycle<br>*ca.* 220 mAh $g^{-1}$ at 200th cycle<br>86% retention over 190 cycles at 50 mA $g^{-1}$ | 210 mAh $g^{-1}$ at 250 mA $g^{-1}$<br>149 mAh $g^{-1}$ at 500 mA $g^{-1}$ |
| hollow carbon nanospheres (ref 51) | 41.5 | *ca.* 20 mAh $g^{-1}$ at 50 mA $g^{-1}$ (10th cycle) | 250 mAh $g^{-1}$ at 10th cycle<br>160 mAh $g^{-1}$ at 100th cycle<br>64% retention over 90 cycles at 100 mA $g^{-1}$ | 168 mAh $g^{-1}$ at 200 mA $g^{-1}$<br>142 mAh $g^{-1}$ at 500 mA $g^{-1}$<br>120 mAh $g^{-1}$ at 1 A $g^{-1}$<br>100 mAh $g^{-1}$ at 2 A $g^{-1}$<br>75 mAh $g^{-1}$ at 5 A $g^{-1}$ |
| carbonized peat moss (ref 54) | 57.5 | 161 mAh $g^{-1}$ at 50 mA $g^{-1}$ (10th cycle) | 284 mAh $g^{-1}$ at 11th cycle<br>255 mAh $g^{-1}$ at 210th cycle<br>90% retention over 200 cycles at 100 mA $g^{-1}$ | 250 mAh $g^{-1}$ at 200 mA $g^{-1}$<br>203 mAh $g^{-1}$ at 500 mA $g^{-1}$<br>150 mAh $g^{-1}$ at 1 A $g^{-1}$<br>106 mAh $g^{-1}$ at 2 A $g^{-1}$<br>66 mAh $g^{-1}$ at 5 A $g^{-1}$ |
| carbon nanofibers (ref 13) | 58.7 | *ca.* 130 mAh $g^{-1}$ at 40 mA $g^{-1}$ (10th cycle) | 200 mAh $g^{-1}$ at 2nd cycle<br>180 mAh $g^{-1}$ at 300th cycle<br>90% retention over 298 cycles at 200 mA $g^{-1}$ | 200 mAh $g^{-1}$ at 200 mA $g^{-1}$<br>160 mAh $g^{-1}$ at 500 mA $g^{-1}$<br>120 mAh $g^{-1}$ at 1 A $g^{-1}$<br>85 mAh $g^{-1}$ at 2 A $g^{-1}$ |
| nanocellular carbon foams (ref 15) | not reported | not reported | 153 mAh $g^{-1}$ at 2nd cycle<br>137 mAh $g^{-1}$ at 300th cycle<br>90% retention over 298 cycles at 100 mA $g^{-1}$ | 140 mAh $g^{-1}$ at 200 mA $g^{-1}$<br>120 mAh $g^{-1}$ at 500 mA $g^{-1}$<br>100 mAh $g^{-1}$ at 1 A $g^{-1}$<br>50 mAh $g^{-1}$ at 5 A $g^{-1}$ |
| porous carbon nanofiber (ref 16) | 53.5 | *ca.* 170 mAh $g^{-1}$ at 50 mA $g^{-1}$ (10th cycle) | 280 mAh $g^{-1}$ at 10th cycle<br>266 mAh $g^{-1}$ at 100th cycle<br>95% retention over 90 cycles at 50 mA $g^{-1}$ | 225 mAh $g^{-1}$ at 500 mA $g^{-1}$<br>200 mAh $g^{-1}$ at 1 A $g^{-1}$<br>164 mAh $g^{-1}$ at 2 A $g^{-1}$<br>90 mAh $g^{-1}$ at 5 A $g^{-1}$ |
| carbon fibers (ref 53) | <40 | 184 mAh $g^{-1}$ (1st cycle) | not reported | not reported |
| hard carbon (ref 14) | 61 | >170 mAh $g^{-1}$ (1st cycle) | 340 mAh $g^{-1}$ at 2nd cycle<br>310 mAh $g^{-1}$ at ~60 mA $g^{-1}$<br>88% retention over 118 cycles at ~30 mA $g^{-1}$ | 300 mAh $g^{-1}$ at 120th cycle<br>240 mAh $g^{-1}$ at ~300 mA $g^{-1}$<br>150 mAh $g^{-1}$ at ~600 mA $g^{-1}$ |

against Li, while a negligible effect when testing against Na (at intermediate and low charging rates where diffusional limitations are not significant). This is one source of the capacity discrepancy between LIBs

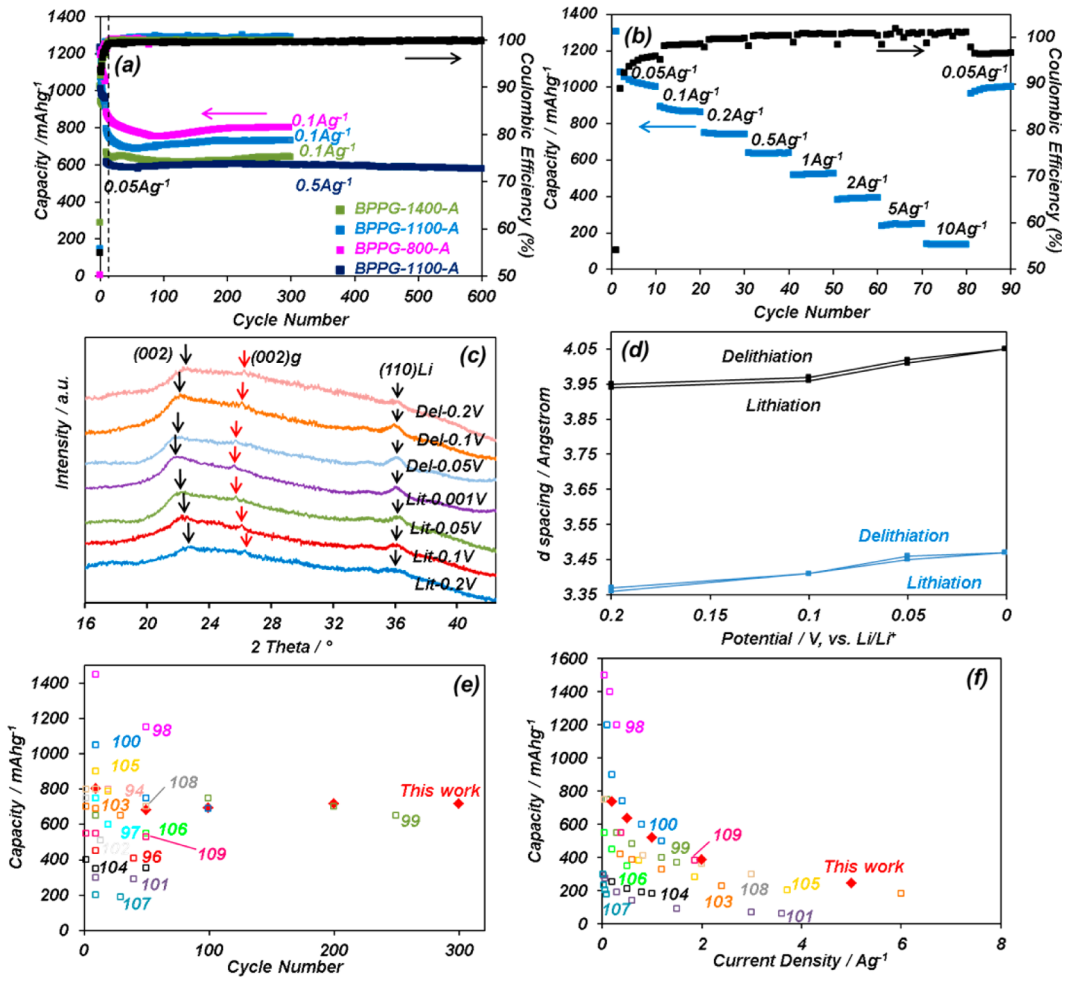


**Figure 4. Electrochemical performance of BPPG, tested in a half-cell against Li. (a) Cycling performance of the BPPG-A electrodes, with the Coulombic efficiency of electrodes being displayed. (b) Rate performance of the BPPG-1100-A electrode. (c) XRD spectra for BPPG-1400-A at different discharge and charge voltages (*versus* Li/Li$^+$). (d) Dependence of the mean graphene interlayer spacing of pseudographite (black line) and graphite (blue line) phases in BPPG-1400-A on the discharge/charge voltage. The electrodes were galvanostatically discharged/charged to 0.2, 0.1, 0.05, and 0.001 V, 10th cycle at 50 mA g$^{-1}$. The actual potential *versus* capacity profiles and a summary of capacity above and below 0.1 V are shown in Figure S18. (e, f) Cycling capacity retention and rate capability comparison of BPPG-1100-A with the state-of-the-art in the literature, tested *versus* Li. (The current density in ref 103 and106 is based on A cm$^{-2}$.) Red diamonds are our results.**

and NIBs and will be shown to be a direct outcome of Li metal nanopore filling. Reversible capacities are 1109 mAh g$^{-1}$ for BPPG-800, 1225 mAh g$^{-1}$ for BPPG-800-A; 1007 mAh g$^{-1}$ for BPPG-1100, 1199 mAh g$^{-1}$ for BPPG-1100-A; and 819 mAh g$^{-1}$ for BPPG-1400, 1021 mAh g$^{-1}$ for BPPG-1400-A. In all three cases the extra capacity due to activation is achieved below 0.1 V (Figure S18). We also hypothesize that the much higher >0.1 V capacity in LIBs *versus* NIBs and the more sloping charge/discharge profiles with a larger hysteresis are directly related to a wider abundance of adsorption sites for Li in the defective graphene layers. The stronger binding sites will have Li absorption occur at a higher voltage ($\Delta G = -nFE$) and will require a large overpotential upon subsequent delithiation of the half-cell.

Figure 4c and d show the dependence of the mean graphene interlayer spacing in the pseudographitic domains and in the equilibrium graphite on the charge/discharge voltage. The sample that was analyzed is BPPG-1400-A. Li intercalation-induced dilation in the pseudographite occurs to a lesser extent than with Na. This difference is in part due to the smaller radius of the Li. We argue that this also another manifestation of proportionally more Li being adsorbed on graphene defects, rather than being intercalated, as the former would add to the overall capacity but not induce systematic lattice dilation. Figure S19a and b show the Raman integral intensity ratio as a function of discharge/charge voltage, demonstrating some Li intercalation-induced ordering of the carbon. The degree of ordering, however, is much less than for Na.

Figure 4c shows a strong lithium metal peak centered at $2\theta \approx 36°$, corresponding to (110)Li. This peak appears upon the reduction of the electrode to 0.2 V and grows more prominent at lower potentials. It also symmetrically shrinks upon delithiation. The unambiguous presence of a (110) metallic Li reflection is a direct evidence of a key contribution of metal nanopore

filling to the overall capacity and agrees with the earlier findings of ref 84. To further confirm this mechanism, we employed XPS (Figure S20) using the same Scotch tape technique to remove the SEI and the top carbon layer. Upon reducing the electrode to 0.001 V, there is a prominent lithium metal peak. Conversely at 2.8 V the metal peak has effectively disappeared. Similarly without using the Scotch tape approach, the presence of the peak with a binding energy of ~55 eV and a considerable intensity in Li 1s spectra even after delithiation to 2.8 V indicates that this peak is attributed to the (Li)carbonate rather than Li metal inside the electrode. SEM images (Figure S21) also confirm that the SEI layer has been successfully removed using the Scotch tape method with a smooth surface compared to the rough one in Figure S21b.

A comparison of the performance of BPPG-1100-A with state-of-the-art carbons is presented in Table S6 and in Figure 4e and f. Extensive research has been done on carbon-based anode materials for LIBs.[95] Carbons included in the comparison are mesoporous carbon,[94] graphene and graphene nanosheets,[96−98,100] carbon nanotubes/graphene,[99] carbon nanotube on graphene paper,[101] graphene nanoribbons,[102] graphene/carbon nanofibers,[103] monolithic carbon,[104] mesoporous carbon,[105] carbon nanotubes on carbon fiber,[106] macroporous carbon,[107] carbon nanospheres,[108] and photothermally reduced graphene,[109] all of them being primarily high surface area materials. We did not include highly doped (*e.g.*, by N, O, or B) carbons in the comparison since these store Li by several additional fundamentally different mechanisms related to reversible ion absorption at the heteroatom functionalities or at the associated defects.[72−74,110] Because of this extra Li storage contribution, the total capacities in such materials are always higher than that for "pure" carbons such the BPPG specimens, undoped graphene, or carbon nanotubes. For instance, recently a 10% N-doped medium surface area carbon was able to achieve a reversible capacity of 1780 mAh $g^{-1}$ in the second cycle.[72] Judging from the table and the figures, the overall performance of BPPG-A specimens is quite favorable in terms of both cycling and high rate capacity retention. This is especially true considering that materials presented in the comparison are all high surface area structures. Figure S22 shows the cycling volumetric capacity of BPPG-1100-A, tested at 50 mA $g^{-1}$. The volumetric capacity, based on the true density of BPPG, is 1460 mAh $cm^{-3}$ after 300 cycles, with 100% cycling CE being achieved by cycle 20.

## CONCLUSIONS

We created a unique low surface area carbon that was derived from banana peels, termed banana peel pseudographite, "BPPG". The materials are composed of pseudographitic arrays possessing a mean graphene interlayer spacing that is 17% dilated with respect to graphite, allowing for facile Na intercalation between the layers. For NIBs, the carbons actually perform as a direct electrochemical analogue to graphite in LIBs in terms of the overall charge storage capacity, superior cycling stability, Coulombic efficiency, a large and nearly flat voltage plateau below 0.1 V, and minimal charge−discharge hysteresis. A wide comparison with literature shows BPPG to possess among the most promising electrochemical performances for a sodium ion battery carbon-based anode. BPPG also serves as a superb electrode for lithium ion batteries, achieving 3 times the capacity of graphite. This may be attributed to a combination of the highly defective graphene in the pseudographitic arrays that reversibly binds Li and the ample near-surface nanopores available for facile underpotential metal deposition.

## METHODS

**Material Synthesis.** The collected biomaterial was extensively washed with DI water, cut into small pieces, and dried at 110 °C overnight in a vacuum oven. Typically 10 g of banana peel precursor was loaded in a tubular furnace for the pyrolysis carbonization process (800−1400 °C for 5 h, heating rate: 5 °C $min^{-1}$) under an argon atmosphere with the flow of 100 sccm $min^{-1}$. The obtained carbon was carefully washed in 20% KOH at 70 °C for 2 h and 2 M HCl at 60 °C for 15 h to remove the remaining impurities. The purified samples were collected by filtration after rinsing further with DI water. Then the carbon was dried at 110 °C overnight in a vacuum oven. Some of the carbonized banana peel pseudographite specimens were further activated at 300 °C for 3 h (at a heating rate of 5 °C $min^{-1}$ in the tubular furnace) in a dry air flow of 50 sccm $min^{-1}$. The obtained activated banana peel pseudographite was first ground and then washed with 2 M HCl and DI water again before use. Commercially purchased battery-grade graphite powder (MTI) and high surface area, high electrical conductivity activated carbon (NORIT Supra) were employed as baselines.

**Electrochemical Testing.** A slurry of 80% BPPG, 10% carbon black (Super-P), and 10% PVDF (binder) in *N*-methylpyrrolidone was coated onto 316L stainless steel spacers of 1.97 $cm^2$ (around 1 mg of active materials on one electrode) and then dried at 110 °C overnight in a vacuum oven. The obtained electrode, polyethene separator, and Na/Li metal counter electrode were assembled into a 2032-type button cell filled with electrolyte, in an Ar-filled glovebox with sub-0.1 ppm water and oxygen contents. The NIB electrolyte was 1 M $NaClO_4$ in 1:1 by volume ethylene carbonate (EC) and diethyl carbonate (DEC). The LIB electrolyte was 1 M $LiPF_6$ in a 1:1:1 volume ratio of EC:DMC:DEC (DMC is dimethyl carbonate). For the samples employed solely for *ex situ* XRD analysis of sodiation/desodiation- or lithiation/delithiation-induced lattice dilation/contraction, carbon black was not included, and the amount of binder was limited to 5 wt %. Cyclic voltammetry was carried out using a Solartron 1470 Multistat system at a scan rate of 0.1 mV $s^{-1}$ (0.001−2.8 V). The charge/discharge measurements were performed using an Arbin BT2000 potentiostat. Electrochemical impedance spectroscopy measurements were also performed using a Solartron 1470E multichannel potentiostat/cell test

system. All electrochemical tests were conducted at room temperature.

**Material Characterization.** The surface area and porous texture of carbon materials were characterized by nitrogen adsorption at 77 K (Quantachrome Autosorb$^{-1}$). Prior to the gas sorption measurements, the samples were outgassed at 250 °C for 4 h under a vacuum. The pore size distributions were evaluated by a nonlocal DFT method using nitrogen adsorption data and assuming slit-pore geometry. To characterize the morphology of the carbon samples, field emission scanning electron microscopy (FE-SEM) (Hitachi S-4800) and transmission electron microscopy (TEM) (JEOL 2200FS, 200 kV) were used. X-ray photoelectron spectroscopy measurements were performed on an ULTRA (Kratos Analytical) spectrometer using monochromatic Al Kα radiation ($h\nu$ = 1486.6 eV) run at 210 W. Before XPS analysis, the samples were dried at 110 °C in a vacuum oven overnight to remove the absorbed water. X-ray diffraction analysis was performed using a Bruker AXS D8 Discover diffractometer with Cu Kα radiation. The Raman spectra were recorded with a confocal microprobe Raman system (Thermo Nicolet Almega XR Raman microscope). Prior to XRD, Raman, and XPS analysis on the partially charged materials, the samples were kept in a glovebox. Sample transfer was done in an Ar-filled sample container, with only minimal ambient exposure occurring prior to analysis.

*Conflict of Interest:* The authors declare no competing financial interest.

*Supporting Information Available:* Figures S1−S22 and Tables S1−S6 as described in the text. This material is available free of charge *via* the Internet at http://pubs.acs.org.

*Acknowledgment.* This work was supported by NSERC Discovery and by NINT NRC.

## REFERENCES AND NOTES


1. Tarascon, J. M. Is Lithium the New Gold? *Nat. Chem.* **2010**, *2*, 510.
2. Pan, H.; Hu, Y. S.; Chen, L. Room-Temperature Stationary Sodium-Ion Batteries for Large-Scale Electric Energy Storage. *Energy Environ. Sci.* **2013**, *6*, 2338.
3. Palomares, V.; Casas-Cabanas, M.; Castillo-Martínez, E.; Han, M. H.; Rojo, T. Update on Na-Based Battery Materials. A Growing Research Path. *Energy Environ. Sci.* **2013**, *6*, 2312.
4. Slater, M. D.; Kim, D.; Lee, E.; Johnson, C. S. Sodium-Ion Batteries. *Adv. Funct. Mater.* **2013**, *23*, 947–958.
5. Cao, Y.; Xiao, L.; Ai, X.; Yang, H. Surface-Modified Graphite as an Improved Intercalating Anode for Lithium-Ion Batteries. *Electrochem. Solid-State Lett.* **2003**, *6*, A30–A33.
6. Lin, Y.; Huang, Z.-H.; Yu, X.; Shen, W.; Zheng, Y.; Kang, F. Mildly Expanded Graphite for Anode Materials of Lithium Ion Battery Synthesized with Perchloric Acid. *Electrochim. Acta* **2014**, *116*, 170–174.
7. Wang, L.; Huang, Y.; Jia, D. Triethyl Orthoformate as a New Film-Forming Electrolytes Solvent for Lithium-Ion Batteries with Graphite Anodes. *Electrochim. Acta* **2006**, *51*, 4950–4955.
8. Peled, E.; Menachem, C.; BarTow, D.; Melman, A. Improved Graphite Anode for Lithium-Ion Batteries; Chemically Bonded Solid Electrolyte Interface and Nanochannel Formation. *J. Electrochem. Soc.* **1996**, *143*, L4–L7.
9. Ge, P. Fouletier, Electrochemical Intercalation of Sodium in Graphite. *Solid State Ionics* **1988**, *28−30*, 1172–1175.
10. Stevens, D. A.; Dahn, J. R. The Mechanisms of Lithium and Sodium Insertion in Carbon Materials. *J. Electrochem. Soc.* **2001**, *148*, A803–A811.
11. Asher, R. C. A Lamellar Compound of Sodium and Graphite. *J. Inorg. Nucl. Chem.* **1959**, *10*, 238–249.
12. Komaba, S.; Murata, W.; Ishikawa, T.; Yabuuchi, N.; Ozeki, T.; Nakayama, T.; Ogata, A.; Gotoh, K.; Fujiwara, K. Electrochemical Na Insertion and Solid Electrolyte Interphase for Hard-Carbon Electrodes and Application to Na-Ion Batteries. *Adv. Funct. Mater.* **2011**, *21*, 3859–3867.
13. Luo, W.; Schardt, J.; Bommier, C.; Wang, B.; Razink, J.; Simonsen, J.; Ji, X. Carbon Nanofibers Derived from Cellulose Nanofibers as a Long-Life Anode Material for Rechargeable Sodium-Ion Batteries. *J. Mater. Chem. A* **2013**, *1*, 10662–10666.
14. Ponrouch, A.; Goni, A. R.; Palacin, M. R. High Capacity Hard Carbon Anodes for Sodium Ion Batteries in Additive Free Electrolyte. *Electrochem. Commun.* **2013**, *27*, 85–88.
15. Shao, Y. Y.; Xiao, J.; Wang, W.; Engelhard, M.; Chen, X. L.; Nie, Z. M.; Gu, M.; Saraf, L. V.; Exarhos, G.; Zhang, J. G.; *et al.* Surface-Driven Sodium Ion Energy Storage in Nanocellular Carbon Foams. *Nano Lett.* **2013**, *13*, 3909–3914.
16. Li, W.; Zeng, L.; Yang, Z.; Gu, L.; Wang, J.; Liu, X.; Cheng, J.; Yu, Y. Free-Standing and Binder-Free Sodium-Ion Electrodes with Ultralong Cycle Life and High Rate Performance Based on Porous Carbon Nanofibers. *Nanoscale* **2014**, *6*, 693–698.
17. Kim, Y.; Park, Y.; Choi, A.; Choi, N.-S.; Kim, J.; Lee, J.; Ry, J. H.; Oh, S. M.; Lee, K. T. An Amorphous Red Phosphorus/Carbon Composite as a Promising Anode Material for Sodium Ion Batteries. *Adv. Mater.* **2013**, *25*, 3045–3049.
18. Li, W. J.; Chou, S.-L.; Wang, J.-Z.; Liu, H.-K.; Dou, S.-X. Simply Mixed Commercial Red Phosphorus and Carbon Nanotube Composite with Exceptionally Reversible Sodium-Ion Storage. *Nano Lett.* **2013**, *13*, 5480–5484.
19. Senguttuvan, P.; Rousse, G.; Arroyo y de Dompablo, M. E.; Vezin, H.; Tarascon, J. M.; Palacín, M. R. Low-Potential Sodium Insertion in a NASICON-Type Structure through the Ti(III)/Ti(II) Redox Couple. *J. Am. Chem. Soc.* **2013**, *135*, 3897–3903.
20. Zhao, L.; Zhao, J. M.; Hu, Y. S.; Li, H.; Zhou, Z. B.; Armand, M.; Chen, L. Q. Disodium Terephthalate ($Na_2C_8H_4O_4$) as High Performance Anode Material for Low-Cost Room-Temperature Sodium-Ion Battery. *Adv. Energy Mater.* **2012**, *2*, 962–965.
21. Park, S. Il; Gocheva, I.; Okada, S.; Yamaki, J.-I. Electrochemical Properties of $NaTi_2(PO_4)_3$ Anode for Rechargeable Aqueous Sodium-Ion Batteries. *J. Electrochem. Soc.* **2011**, *158*, A1067–A1070.
22. Park, Y.; Shin, D. S.; Woo, S. H.; Choi, N. S.; Shin, K. H.; Oh, S. M.; Lee, K. T.; Hong, S. Y. Sodium Terephthalate as an Organic Anode Material for Sodium Ion Batteries. *Adv. Mater.* **2012**, *24*, 3562–3567.
23. Wang, W.; Yu, C.; Lin, Z.; Hou, J.; Zhu, H.; Jiao, S. Microspheric $Na_2Ti_3O_7$ Consisting of Tiny Nanotubes: An Anode Material for Sodium-Ion Batteries with Ultrafast Charge−Discharge Rates. *Nanoscale* **2013**, *5*, 594–599.
24. Pan, H. L.; Lu, X.; Yu, X. Q.; Hu, Y. S.; Li, H.; Yang, X. Q.; Chen, L. Q. Sodium Storage and Transport Properties in Layered $Na_2Ti_3O_7$ for Room-Temperature Sodium-Ion Batteries. *Adv. Energy Mater.* **2013**, *3*, 1186–1194.
25. Wu, L.; Buchholz, D.; Bresser, D.; Chagas, L. G.; Passerini, S. Anatase $TiO_2$ Nanoparticles for High Power Sodium-Ion Anodes. *J. Power Sources* **2014**, *251*, 379–385.
26. Alcántara, R.; Jaraba, M.; Lavela, P.; Tirado, J. L. $NiCo_2O_4$ Spinel: First Report on a Transition Metal Oxide for the Negative Electrode of Sodium-Ion Batteries. *Chem. Mater.* **2002**, *14*, 2847–2848.
27. Xiong, H.; Slater, M. D.; Balasubramanian, M.; Johnson, C. S.; Rajh, T. Amorphous $TiO_2$ Nanotube Anode for Rechargeable Sodium Ion Batteries. *J. Phys. Chem. Lett.* **2011**, *2*, 2560–2565.
28. Xu, Y.; Lotfabad, E. M.; Wang, H. L.; Farbod, B.; Xu, Z. W.; Kohandehghan, A.; Mitlin, D. Nanocrystalline Anatase $TiO_2$: A New Anode Material for Rechargeable Sodium Ion Batteries. *Chem. Commun.* **2013**, *49*, 8973–8975.
29. Kim, K.-T.; Ali, G.; Chung, K. Y.; Yoon, C. S.; Yashiro, H.; Sun, Y. K.; Sun, Y.-K.; Lu, J.; Amine, K.; Myung, S.-T. Anatase Titania Nanorods as an Intercalation Anode Material for Rechargeable Sodium Batteries. *Nano Lett.* **2014**, *14*, 416–422.
30. Hariharan, S.; Saravanan, K.; Ramar, V.; Balaya, P. A Rationally Designed Dual Role Anode Material for Lithium-Ion and Sodium-Ion Batteries: Case Study of Eco-Friendly $Fe_3O_4$. *Phys. Chem. Chem. Phys.* **2013**, *15*, 2945–2953.

31. Li, X.; Hasan, M. M.; Hector, A. L.; Owen, J. R. Performance of Nanocrystalline $Ni_3N$ as a Negative Electrode for Sodium-Ion Batteries. *J. Mater. Chem. A* **2013**, *1*, 6441–6445.
32. Baggetto, L.; Ganesh, P.; Sun, C. N.; Meisner, R. A.; Zawodzinski, T. A.; Veith, G. M. Intrinsic Thermodynamic and Kinetic Properties of Sb Electrodes for Li-Ion and Na-Ion Batteries: Experiment and Theory. *J. Mater. Chem. A* **2013**, *1*, 7985–7994.
33. Zhu, H. L.; Jia, Z.; Chen, Y. C.; Weadock, N.; Wan, J. Y.; Vaaland, O.; Han, X. G.; Li, T.; Hu, L. B. Tin Anode for Sodium-Ion Batteries Using Natural Wood Fiber as a Mechanical Buffer and Electrolyte Reservoir. *Nano Lett.* **2013**, *13*, 3093–3100.
34. Baggetto, L.; Ganesh, P.; Meisner, R. P.; Unocic, R. R.; Jumas, J. C.; Bridges, C. A.; Veith, G. M. Characterization of Sodium Ion Electrochemical Reaction with Tin Anodes: Experiment and Theory. *J. Power Sources* **2013**, *234*, 48–59.
35. Xiao, L. F.; Cao, Y. L.; Xiao, J.; Wang, W.; Kovarik, L.; Nie, Z. M.; Liu, J. High Capacity, Reversible Alloying Reactions in SnSb/C Nanocomposites for Na-Ion Battery Applications. *Chem. Commun.* **2012**, *48*, 3321–3323.
36. Wang, J. W.; Liu, X. H.; Mao, S. X.; Huang, J. Y. Microstructural Evolution of Tin Nanoparticles during *in Situ* Sodium Insertion and Extraction. *Nano Lett.* **2012**, *12*, 5897–5902.
37. Wu, L.; Hu, X.; Qian, J.; Pei, F.; Wu, F.; Mao, R.; Ai, X.; Yang, H.; Cao, Y. Sb–C Nanofibers with Long Cycle Life as an Anode Material for High-Performance Sodium-Ion Batteries. *Energy Environ. Sci.* **2014**, *7*, 323.
38. Zhu, Y.; Han, X.; Xu, Y.; Liu, Y.; Zheng, S.; Xu, K.; Hu, L.; Wang, C. Electrospun Sb/C Fibers for a Stable and Fast Sodium-Ion Battery Anode. *ACS Nano* **2013**, *7*, 6378–6386.
39. Han, X.; Liu, Y.; Jia, Z.; Chen, Y.-C.; Wan, J.; Weadock, N.; Gaskell, K. J.; Li, T.; Hu, L. Atomic-Layer-Deposition Oxide Nanoglue for Sodium Ion Batteries. *Nano Lett.* **2014**, *14*, 139–147.
40. Liu, Y.; Xu, Y.; Zhu, Y.; Culver, J. N.; Lundgren, C. A.; Xu, K.; Wang, C. Tin-Coated Viral Nanoforests as Sodium-Ion Battery Anodes. *ACS Nano* **2013**, *7*, 3627–3634.
41. Jung, S. C.; Jung, D. S.; Choi, J. W.; Han, Y.-K. Atom-Level Understanding of the Sodiation Process in Silicon Anode Material. *J. Phys. Chem. Lett.* **2014**, *5*, 1283–1288.
42. Farbod, B.; Cui, K.; Kalisvaart, W. P.; Kupsta, M.; Zahiri, B.; Kohandehghan, A.; Memarzadeh, E.; Li, Z.; Luber, E. J.; Mitlin, D. Anodes for Sodium Ion Batteries based on Tin–Germanium–Antimony Alloys. *ACS Nano* **2014**, *8*, 4415–4429.
43. Qian, J.; Xiong, Y.; Cao, Y.; Ai, X.; Yang, H. Synergistic Na-Storage Reactions in $Sn_4P_3$ as a High-Capacity, Cycle-stable Anode of Na-Ion Batteries. *Nano Lett.* **2014**, *14*, 1865–1869.
44. Ji, L.; Gu, M.; Shao, Y.; Li, X.; Engelhard, M. H.; Arey, B. W.; Wang, W.; Nie, Z.; Xiao, J.; Wang, C.; *et al*. Controlling SEI Formation on SnSb-Porous Carbon Nanofibers for Improved Na Ion Storage. *Adv. Mater.* **2014**, *26*, 2901–2908.
45. David, L.; Bhandavat, R.; Singh, G. $MoS_2$/Graphene Composite Paper for Sodium-Ion Battery Electrodes. *ACS Nano* **2014**, *8*, 1759–1770.
46. Datta, D.; Li, J.; Shenoy, V. B. Defective Graphene as a High-Capacity Anode Material for Na- and Ca-Ion Batteries. *ACS Appl. Mater. Interfaces* **2014**, *6*, 1788–1795.
47. Naguib, M.; Mochalin, V. N.; Barsoum, M. W.; Gogotsi, Y. 25th Anniversary Article: MXenes: A New Family of Two-Dimensional Materials. *Adv. Mater.* **2014**, *26*, 992–1005.
48. Lukatskaya, M. R.; Mashtalir, O.; Ren, C. E.; Dall'Agnese, Y.; Rozier, P.; Taberna, P. L.; Naguib, M.; Simon, P.; Barsoum, M. W.; Gogotsi, Y. Cation Intercalation and High Volumetric Capacitance of Two-Dimensional Titanium Carbide. *Science* **2013**, *341*, 1502–1505.
49. Naguib, M.; Halim, J.; Lu, J.; Cook, K. M.; Hultman, L.; Gogotsi, Y.; Barsoum, M. W. New Two-Dimensional Niobium and Vanadium Carbides as Promising Materials for Li-Ion Batteries. *J. Am. Chem. Soc.* **2013**, *135*, 15966–15969.
50. Mashtalir, O.; Naguib, M.; Mochalin, V. N.; Dall'Agnese, Y.; Heon, M.; Barsoum, M. W.; Gogotsi, Y. Intercalation and Delamination of Layered Carbides and Carbonitrides. *Nat. Commun.* **2013**, *4*, 1716.
51. Tang, K.; Fu, L. J.; White, R. J.; Yu, L. H.; Titirici, M. M.; Antonietti, M.; Maier, J. Hollow Carbon Nanospheres with Superior Rate Capability for Sodium-Based Batteries. *Adv. Energy Mater.* **2012**, *2*, 873–877.
52. Cao, Y.; Xiao, L.; Sushko, M. L.; Wang, W.; Schwenzer, B.; Xiao, J.; Nie, Z.; Saraf, L. V.; Yang, Z.; Liu, J. Sodium Ion Insertion in Hollow Carbon Nanowires for Battery Applications. *Nano Lett.* **2012**, *12*, 3783–3787.
53. Thomas, P.; Billaud, D. Effect of Mechanical Grinding of Pitch-Based Carbon Fibers and Graphite on their Electrochemical Sodium Insertion Properties. *Electrochim. Acta* **2000**, *46*, 39–47.
54. Ding, J.; Wang, H.; Li, Z.; Kohandehghan, A.; Cui, K.; Xu, Z.; Zahiri, B.; Tan, X.; Memarzadeh Lotfabad, E.; Olsen, B. C.; *et al*. Carbon Nanosheet Frameworks Derived from Peat Moss as High Performance Sodium Ion Battery Anodes. *ACS Nano* **2013**, *7*, 11004–11015.
55. Zhou, X.; Guo, Y.-G. Highly Disordered Carbon as a Superior Anode Material for Room-Temperature Sodium-Ion Batteries. *ChemElectroChem* **2014**, *1*, 83–86.
56. Wang, H.-G.; Wu, Z.; Meng, F. I.; Ma, D.-L.; Huang, X.-L.; Wang, L.-M.; Zhang, X.-B. Nitrogen-Doped Porous Carbon Nanosheets as Low-Cost, High-Performance Anode Material for Sodium-Ion Batteries. *ChemSusChem* **2013**, *6*, 56–60.
57. Fu, L.; Tang, K.; Song, K.; van Aken, P. A.; Yu, Y.; Maier, J. Nitrogen Doped Porous Carbon Fibres as Anode Materials for Sodium Ion Batteries with Excellent Rate Performance. *Nanoscale* **2014**, *6*, 1384–1389.
58. Gui, Z.; Zhu, H.; Gillette, E.; Han, X.; Rubloff, G. W.; Hu, L.; Lee, S. B. Natural Cellulose Fiber as Substrate for Supercapacitor. *ACS Nano* **2013**, *7*, 6037–6046.
59. Chen, X.; Zhu, H.; Liu, C.; Chen, Y.-C.; Weadock, N.; Rubloff, G.; Hu, L. Role of Mesoporosity in Cellulose Fibers for Paper-Based Fast Electrochemical Energy Storage. *J. Mater. Chem. A* **2013**, *1*, 8201–8208.
60. Li, N.; Chen, Z.; Ren, W.; Li, F.; Cheng, H. M. Flexible Graphene-Based Lithium Ion Batteries with Ultrafast Charge and Discharge Rates. *Proc. Natl. Acad. Sci. U.S.A.* **2012**, *109*, 17360–17365.
61. Lee, S.-H.; Sridhar, V.; Jung, J.-H.; Karthikeyan, K.; Lee, Y.-S.; Mukherjee, R.; Koratkar, N.; Oh, I.-K. Graphene-Nanotube-Iron Hierarchical Nanostructure as Lithium Ion Battery Anode. *ACS Nano* **2013**, *7*, 4244–4251.
62. Li, L.; Zhou, G.; Weng, Z.; Shan, X.-Y.; Li, F.; Cheng, H.-M. Monolithic $Fe_2O_3$/Graphene Hybrid for Highly Efficient Lithium Storage and Arsenic Removal. *Carbon* **2014**, *67*, 500–507.
63. Pol, V. G.; Lee, E.; Zhou, D.; Dogan, F.; Calderon-Moreno, J. M.; Johnson, C. S. Spherical Carbon as a New High-Rate Anode for Sodium-ion Batteries. *Electrochim. Acta* **2014**, *127*, 61–67.
64. Wenzel, S.; Hara, T.; Janek, J.; Adelhelm, P. Room-Temperature Sodium-Ion Batteries: Improving the Rate Capability of Carbon Anode Materials by Templating Strategies. *Energy Environ. Sci.* **2011**, *4*, 3342–3345.
65. Wang, Y.-X.; Chou, S.-L.; Liu, H.-K.; Dou, S.-X. Reduced Graphene Oxide with Superior Cycling Stability and Rate Capability for Sodium Storage. *Carbon* **2013**, *57*, 202–208.
66. Lin, B. H.; Yen, S. T.; Huang, C. L.; Smith, T. A. US Demand for Organic and Conventional Fresh Fruits: The Roles of Income and Price. *Sustainability* **2009**, *1*, 464–478.
67. Annadurai, G.; Juang, R.-S.; Lee, D.-J. Adsorption of Heavy Metals from Water Using Banana and Orange Peels. *Water Sci. Technol.* **2003**, *47*, 185–190.
68. Annadurai, G.; Juang, R.-S.; Lee, D.-J. Use of Cellulose-Based Wastes for Adsorption of Dyes from Aqueous Solutions. *J. Hazard. Mater.* **2002**, *92*, 263–274.
69. Achak, M.; Hafidi, A.; Ouazzani, N.; Sayadi, S.; Mandi, L. Low Cost Biosorbent "Banana Peel" for the Removal of

Phenolic Compounds from Olive Mill Wastewater: Kinetic and Equilibrium Studies. *J. Hazard. Mater.* **2009**, *166*, 117–125.
70. Subramanian, V.; Luo, C.; Stephan, A. M.; Nahm, K. S.; Thomas, S.; Wei, B. Supercapacitors from Activated Carbon Derived from Banana Fibers. *J. Phys. Chem. C* **2007**, *111*, 7527–7531.
71. Lva, Y.; Gana, L.; Liua, M.; Xionga, W.; Xua, Z.; Zhua, D.; Wright, D. S. A Self-Template Synthesis of Hierarchical Porous Carbon Foams Based on Banana Peel for Supercapacitor Electrodes. *J. Power Sources* **2012**, *29*, 152–157.
72. Li, Z.; Xu, Z.; Tan, X.; Wang, H.; Holt, C. M. B.; Stephenson, T.; Olsen, B. C.; Mitlin, D. Mesoporous Nitrogen-Rich Carbons Derived from Protein for Ultra-High Capacity Battery Anodes and Supercapacitors. *Energy Environ. Sci.* **2013**, *6*, 871–878.
73. Wu, Z. S.; Ren, W. C.; Xu, L.; Li, F.; Cheng, H. M. Doped Graphene Sheets as Anode Materials with Superhigh Rate and Large Capacity for Lithium Ion Batteries. *ACS Nano* **2011**, *5*, 5463–5471.
74. Wang, H.; Zhang, C.; Liu, Z.; Wang, L.; Han, P.; Xu, H.; Zhang, K.; Dong, S.; Yao, J.; Cui, G. Nitrogen-Doped Graphene Nanosheets with Excellent Lithium Storage Properties. *J. Mater. Chem.* **2011**, *21*, 5430–5434.
75. Emaga, T. H.; Robert, C.; Ronkart, S. N.; Wathelet, B.; Paquot, M. Dietary Fibre Components and Pectin Chemical Features of Peels during Ripening in Banana and Plantain Varieties. *Bioresour. Technol.* **2008**, *99*, 4346–4354.
76. Titirici, M. M.; Thomas, A.; Yu, S.-H.; Müller, J.-O.; Antonietti, M. A Direct Synthesis of Mesoporous Carbons with Bicontinuous Pore Morphology from Crude Plant Material by Hydrothermal Carbonization. *Chem. Mater.* **2007**, *19*, 4205–4212.
77. Emaga, T.; Bindelle, J.; Agneesens, R.; Buldgen, A.; Wathelet, B.; Paquot, M. Ripening Influences Banana and Plantain Peels Composition and Energy Content. *Trop. Anim. Health Prod.* **2011**, *43*, 171–177.
78. Dahn, J. R.; Zheng, T.; Liu, Y.; Xue, J. S. Mechanisms for Lithium Insertion in Carbonaceous Materials. *Science* **1995**, *270*, 590–593.
79. Portet, C.; Yushin, G.; Gogotsi, Y. Electrochemical Performance of Carbon Onions, Nanodiamonds, Carbon Black and Multiwalled Nanotubes in Electrical Double Layer Capacitors. *Carbon* **2007**, *45*, 2511–2518.
80. Wang, Z.; Qie, L.; Yuan, L.; Zhang, W.; Hu, X.; Huang, Y. Functionalized N-Doped Interconnected Carbon Nanofibers as an Anode Material for Sodium-Ion Storage with Excellent Performance. *Carbon* **2013**, *55*, 328–334.
81. Stevens, D. A.; Dahn, J. R. High Capacity Anode Materials for Rechargeable Sodium-Ion Batteries. *J. Electrochem. Soc.* **2000**, *147*, 1271–1273.
82. Wang, C. S.; Wu, G. T.; Li, W. Z. Lithium Insertion in Ball-Milled Graphite. *J. Power Sources* **1998**, *76*, 1–10.
83. Datta, D.; Li, J.; Shenoy, V. B. Defective Graphene as a High-Capacity Anode Material for Na- and Ca-Ion Batteries. *ACS Appl. Mater. Interfaces* **2014**, *6*, 1788–1795.
84. Mukherjee, R.; Thomas, A. V.; Datta, D.; Singh, E.; Li, J.; Eksik, O.; Shenoy, V. B.; Koratkar, N. Defect-Induced Plating of Lithium Metal within Porous Graphene Networks. *Nat. Commun.* **2014**, *5*, 3710.
85. Liu, Y.; Artyukhov, V. I.; Liu, M.; Harutyunyan, A. R.; Yakobson, B. I. Feasibility of Lithium Storage on Graphene and Its Derivatives. *J. Phys. Chem. Lett.* **2013**, *4*, 1737–1742.
86. Zhou, L.-J.; Hou, Z. F.; Wu, L.-M. First-Principles Study of Lithium Adsorption and Diffusion on Graphene with Point Defects. *J. Phys. Chem. C* **2012**, *116*, 21780–21787.
87. Billaud, D.; Henry, F. X.; Willmann, P. Electrochemical Synthesis of Binary Graphite-Lithium Intercalation Compounds. *Mater. Res. Bull.* **1993**, *28*, 477–483.
88. NIST XPS database at http://srdata.nist.gov/xps/Default.aspx.
89. Simon, P.; Gogotsi, Y.; Dunn, B. Where Do Batteries End and Supercapacitors Begin? *Science* **2014**, *343*, 1210–1211.
90. Levi, M. D.; Aurbach, D. Diffusion Coefficients of Lithium Ions during Intercalation into Graphite Derived from the Simultaneous Measurements and Modeling of Electrochemical Impedance and Potentiostatic Intermittent Titration Characteristics of Thin Graphite Electrodes. *J. Phys. Chem. B* **1997**, *10*, 4641–4647.
91. Banhart, F.; Kotakoski, J.; Krasheninnikov, A. V. Structural Defects in Graphene. *ACS Nano* **2011**, *5*, 26–41.
92. Carlsson, J. M.; Scheffler, M. Structural, Electronic, and Chemical Properties of Nanoporous Graphene. *Phys. Rev. Lett.* **2006**, *96*, 046806.
93. Alcantara, R.; Jimenez-Mateos, J. M.; Lavela, P.; Tirado, J. L. Carbon Black: A Promising Electrode Material for Sodium-Ion Batteries. *Electrochem. Commun.* **2001**, *3*, 639–642.
94. Zhou, H.; Zhu, S.; Hibino, M.; Honma, I.; Ichihara, M. Lithium Storage in Ordered Mesoporous Carbon (CMK-3) with High Reversible Specific Energy Capacity and Good Cycling Performance. *Adv. Mater.* **2003**, *15*, 2107–2111.
95. Mukherjee, R.; Krishnan, R.; Lu, T.-M.; Koratkar, N. Nanostructured Electrodes for High-Power Lithium Ion Batteries. *Nano Energy* **2012**, *1*, 518–533.
96. Kumar, A.; Reddy, A. L. M.; Mukherjee, A.; Dubey, M.; Zhan, X.; Singh, N.; Ci, L.; Billups, W. E.; Nagurny, J.; Mital, G.; *et al.* Direct Synthesis of Lithium-Intercalated Graphene for Electrochemical Energy Storage Application. *ACS Nano* **2011**, *5*, 4345–4349.
97. Yoo, E.; Kim, J.; Hosono, E.; Zhou, H.-S.; Kudo, T.; Honma, I. Large Reversible Li Storage of Graphene Nanosheet Families for Use in Rechargeable Lithium Ion Batteries. *Nano Lett.* **2008**, *8*, 2277–2282.
98. Yin, S.; Zhang, Y.; Kong, J.; Zou, C.; Li, C. M.; Lu, X.; Ma, J.; Boey, F. Y. C.; Chen, X. Assembly of Graphene Sheets into Hierarchical Structures for High-Performance Energy Storage. *ACS Nano* **2011**, *5*, 3831–3838.
99. Wang, W.; Ruiz, I.; Guo, S.; Favors, Z.; Hosseini Bay, H.; Ozkan, M.; Ozkan, C. S. Hybrid Carbon Nanotube and Graphene Nanostructures for Lithium Ion Battery Anodes. *Nano Energy* **2014**, *3*, 113–118.
100. Li, X.; Hu, Y.; Liu, J.; Lushington, A.; Li, R.; Sun, X. Structurally Tailored Graphene Nanosheets as Lithium Ion Battery Anodes: An Insight to Yield Exceptionally High Lithium Storage Performance. *Nanoscale* **2013**, *5*, 12607–12615.
101. Li, S.; Luo, Y.; Lv, W.; Yu, W.; Wu, S.; Hou, P.; Yang, Q.; Meng, Q.; Liu, C.; Cheng, H.-M. Vertically Aligned Carbon Nanotubes Grown on Graphene Paper as Electrodes in Lithium-Ion Batteries and Dye-Sensitized Solar Cells. *Adv. Energy Mater.* **2011**, *1*, 486–490.
102. Bhardwaj, T.; Antic, A.; Pavan, B.; Barone, V.; Fahlman, B. D. Enhanced Electrochemical Lithium Storage by Graphene Nanoribbons. *J. Am. Chem. Soc.* **2010**, *132*, 12556–12558.
103. Fan, Z. J.; Yan, J.; Wei, T.; Ning, G.-Q.; Zhi, L.-J.; Liu, J.-C.; Cao, D.-X.; Wang, G.-L.; Wei, F. Nanographene-Constructed Carbon Nanofibers Grown on Graphene Sheets by Chemical Vapor Deposition: High-Performance Anode Materials for Lithium Ion Batteries. *ACS Nano* **2011**, *5*, 2787–2794.
104. Hao, G.-P.; Han, F.; Guo, D.-C.; Fan, R.-J.; Xiong, G.; Li, W.-C.; Lu, A.-H. Monolithic Carbons with Tailored Crystallinity and Porous Structure as Lithium-Ion Anodes for Fundamental Understanding Their Rate Performance and Cycle Stability. *J. Phys. Chem. C* **2012**, *116*, 10303–10311.
105. Guo, B.; Wang, X.; Fulvio, P. F.; Chi, M.; Mahurin, S. M.; Sun, X. G.; Dai, S. Soft-Templated Mesoporous Carbon-Carbon Nanotube Composites for High Performance Lithium-ion Batteries. *Adv. Mater.* **2011**, *23*, 4661–4666.
106. Chen, J.; Wang, J. Z.; Minett, A. I.; Liu, Y.; Lynam, C.; Liu, H.; Wallace, G. G. Carbon Nanotube Network Modified Carbon Fibre Paper for Li-Ion Batteries. *Energy Environ. Sci.* **2009**, *2*, 393–396.
107. Lee, B. K. T.; Lytle, J. C.; Ergang, N. S.; Oh, S. M.; Stein, A. Synthesis and Rate Performance of Monolithic Macroporous Carbon Electrodes for Lithium-Ion Secondary Batteries. *Adv. Funct. Mater.* **2005**, *15*, 547–556.
108. Chen, Y.; Lu, Z.; Zhou, L.; Mai, Y.-W.; Huang, H. *In Situ* Formation of Hollow Graphitic Carbon Nanospheres in

Electrospun Amorphous Carbon Nanofibers for High-Performance Li-Based Batteries. *Nanoscale* **2012**, *4*, 6800–6805.
109. Mukherjee, R.; Thomas, A. V.; Krishnamurthy, A.; Koratkar, N. Photothermally Reduced Graphene as High-Power Anodes for Lithium-Ion Batteries. *ACS Nano* **2012**, *6*, 7867–7878.
110. Qie, L.; Chen, W. M.; Wang, Z. H.; Shao, Q. G.; Li, X.; Yuan, L. X.; Hu, X. L.; Zhang, W. X.; Huang, Y. H. Nitrogen-Doped Porous Carbon Nanofiber Webs as Anodes for Lithium Ion Batteries with a Superhigh Capacity and Rate Capability. *Adv. Mater.* **2012**, *24*, 2047–2050.